

A Newly Identified Degeneracy Keeps the Planetary Interpretation Viable for OGLE-2011-BLG-0950

JIYUAN ZHANG,¹ WEICHENG ZANG,² ANDRZEJ UDALSKI,³ HONGJING YANG,^{4,2} SHUDE MAO,² MICHAŁ K. SZYMAŃSKI,³ IGOR SOSZYŃSKI,³ RADOSŁAW POLESKI,³ KRZYSZTOF ULACZYK,⁵ PAWEŁ PIETRUKOWICZ,³ SZYMON KOZŁOWSKI,³ JAN SKOWRON,³ PRZEMEK MRÓZ,³ SEAN TERRY,^{6,7} AND ANDREW GOULD^{8,9}

¹Department of Astronomy, Tsinghua University, Beijing 100084, China

²Department of Astronomy, Westlake University, Hangzhou 310030, Zhejiang Province, China

³Astronomical Observatory, University of Warsaw, Al. Ujazdowskie 4, 00-478 Warsaw, Poland

⁴Westlake Institute for Advanced Study, Hangzhou 310030, Zhejiang Province, China

⁵Department of Physics, University of Warwick, Gibbet Hill Road, Coventry, CV4 7AL, UK

⁶Code 667, NASA Goddard Space Flight Center, Greenbelt, MD 20771, USA

⁷Department of Astronomy, University of Maryland, College Park, MD 20742, USA

⁸Max-Planck-Institute for Astronomy, Königstuhl 17, 69117 Heidelberg, Germany

⁹Department of Astronomy, Ohio State University, 140 W. 18th Ave., Columbus, OH 43210, USA

ABSTRACT

The microlensing event OGLE-2011-BLG-0950 exhibits the well-known “Planet/Binary” degeneracy, in which distinct lens configurations produce similar light curves but imply substantially different mass ratios between the lens components. A previous study suggested that high-resolution imaging could break this degeneracy through differences in the lens-source relative proper motion. In this work, we identify a new planetary model for this event that arises from a newly identified degeneracy, simultaneously reproducing the observed light curve and remaining consistent with the relative proper motion measured from high-resolution imaging. By combining constraints from the light-curve modeling and high-resolution observations, we infer a lens system consisting of a $\sim 1 M_{\odot}$ host star orbited by a $\sim 1.5 M_{\text{Jup}}$ planet, with a projected separation of about 2 or 8 au, subject to the “Close/Wide” degeneracy. Our reanalysis of the color-magnitude diagram further indicates that the source star has unresolved companions that contribute non-negligible blended light, highlighting the importance of carefully accounting for source and lens companions in future Roman microlensing analyses. Finally, we show that adopting a single mass–luminosity relation significantly underestimates the uncertainties in the inferred lens properties for host masses $\gtrsim 1 M_{\odot}$.

1. INTRODUCTION

The gravitational microlensing technique is most sensitive to planets located near or beyond Jupiter-like orbital separations (Mao & Paczynski 1991; Gould & Loeb 1992; Bennett & Rieh 1996). To date, six homogeneous planet samples have been produced by microlensing surveys (Gould et al. 2010; Cassan et al. 2012; Suzuki et al. 2016; Shvartzvald et al. 2016; Poleski et al. 2021; Zang et al. 2025). Among these, Gould et al. (2010) provided the first measurement of the planet occurrence rate from microlensing observations. In addition, Zang et al. (2025) presented the largest sample to date, comprising 63 planets, and identified a bimodal distribution in the planet-to-host mass ratio (q), with two distinct populations corresponding to super-Earths/Neptune-like planets and gas giants.

Corresponding author: Jiyuan Zhang, Weicheng Zang
 zhangjy22@mails.tsinghua.edu.cn, zangweicheng@westlake.edu.cn

Degeneracies are common in microlensing planet detections. Some degeneracies, such as the “Close/Wide” degeneracy, for which two planetary solutions are approximately related by $s \leftrightarrow s^{-1}$ (Griest & Safizadeh 1998; Dominik 1999; An 2005), where s is the projected separation between the planet and host in units of the Einstein radius, and the “inner/outer” degeneracy (Gaudi & Gould 1997), for which the source trajectory passes either inside (“inner”) or outside (“outer”) the planetary caustic(s) relative to the central caustic, generally yield similar values of the mass ratio and therefore do not significantly affect statistical studies of the planetary mass-ratio function. However, there are two types of degeneracy that frequently arise in planetary events that can introduce substantial ambiguities.

The first is the binary-lens single-source (2L1S) versus single-lens binary-source (1L2S) degeneracy (Gaudi 1998). This degeneracy typically arises in events exhibiting bump-like anomalies, which can also be reproduced by a 1L2S configuration for which a much fainter secondary source passes

closer to the lens than the primary source. Three approaches are commonly employed to discriminate between the two interpretations. First, one can compare the goodness of fit by examining the χ^2 difference between the 2L1S and 1L2S models. Second, the two-source scenario generally predicts a color difference between the primary and secondary sources due to their differing luminosities (Mao & Paczynski 1991; Gaudi 1998). Third, if finite-source effects are detected for the secondary source and imply an unrealistically low lens-source relative proper motion, the 1L2S model can be rejected. Nevertheless, in many cases the 1L2S interpretation cannot be definitively excluded. For example, during the construction of the statistical sample by Zang et al. (2025), nine candidate planetary events were excluded because of the unresolved 2L1S/1L2S degeneracy.

The second is the “Planet/Binary” degeneracy (Han & Gaudi 2008), which frequently arises in high-magnification events and can lead to substantially different inferred values of q , spanning both the planetary and stellar-binary regimes. In the analysis of Zang et al. (2025), three events affected by this degeneracy were therefore excluded from the mass-ratio function study. In some cases, the planetary interpretation yields a well-constrained measurement of the lens-source relative proper motion, μ_{rel} , whereas the stellar-binary model provides only a weak lower limit on μ_{rel} (see the summary in Zhang et al. 2025, hereafter Z25). High-resolution imaging obtained with space-based telescopes or ground-based adaptive optics (AO) facilities can sometimes discriminate between the two scenarios. If the lens and source are resolved and the measured separation implies a μ_{rel} that is inconsistent with the planetary models, the planetary interpretation can be rejected. This approach was demonstrated by Terry et al. (2022) (hereafter T22) for OGLE-2011-BLG-0950, for which Keck AO imaging yielded a heliocentric lens-source relative proper motion that, after transformation to the geocentric frame, corresponds to $\mu_{\text{rel},G} = 4.06 \pm 0.22 \text{ mas yr}^{-1}$, in clear disagreement with $\mu_{\text{rel},G} = 1.05 \pm 0.20 \text{ mas yr}^{-1}$ predicted by the planetary model based on their light curve and color-magnitude diagram analysis.

Recently, Z25 identified a new “Planet Finite/Planet Point” degeneracy in events showing the “Planet/Binary” degeneracy. The “Planet Finite” solutions have well-detected finite-source effects and therefore yield tightly constrained μ_{rel} that can be strongly tested with high-resolution imaging, whereas the degenerate “Planet Point” solutions, similar to the stellar-binary models, exhibit weak constraints on finite-source effects and, consequently, on the relative proper motion. As a result, the “Planet Point” branch generally cannot be ruled out by high-resolution imaging. Motivated by this newly identified degeneracy, we re-modeled the light curve of OGLE-2011-BLG-0950 and confirmed that such “Planet Point” solutions are also present in this event, in addition to

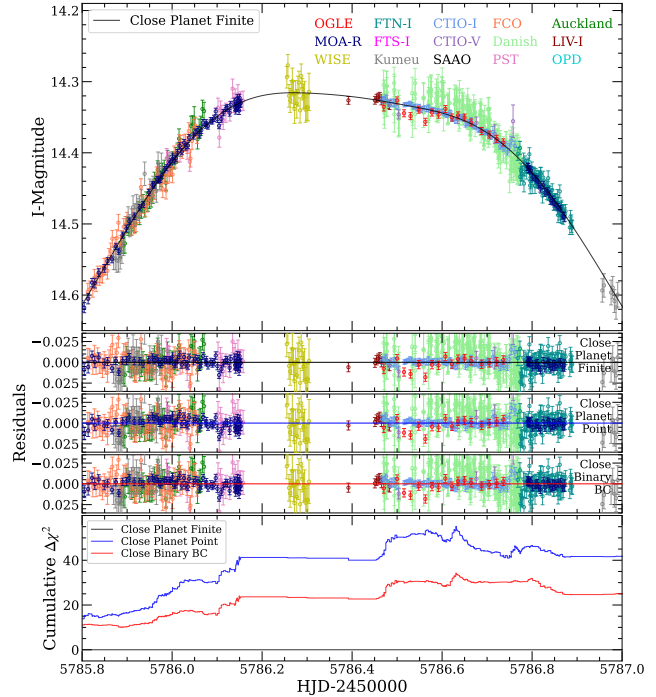


Figure 1. Observed light curves and 2L1S lensing models for OGLE-2011-BLG-0950. The various data sets are shown in different colors. The asymmetric peak is explained by 2L1S models. The black curve in the top panel represents the “Close Planet Finite” solution, which yields the lowest χ^2 among the tested 2L1S models. Residuals for the best-fit “Planet Finite”, “Planet Point”, and “Binary” solutions are shown in the second through fourth panels, respectively. The bottom panel presents the cumulative $\Delta\chi^2$ distributions of these solutions relative to the “Close Planet Finite” solution. The lensing parameters for all 2L1S solutions are listed in Table 1.

the previously published planetary solution that corresponds to the “Planet Finite” branch and is ruled out by the Keck AO relative proper motion constraint, thereby keeping the planetary interpretation viable. In Section 2, we describe the light-curve analysis of this event. In Sections 3 and 4, we present a detailed assessment of the source properties and derive the lens properties. Finally, in Section 5, we discuss the broader implications and potential directions for future work.

2. LIGHT-CURVE ANALYSIS

Figure 1 displays the observed light curve and the best-fit 2L1S models for OGLE-2011-BLG-0950¹. The data used

¹ The astute reader will note that, compared to T22, the data in the top panel of Figure 1 are flipped with respect to the model: epochs where the data lie brighter than the model in our plot lie fainter than the model in T22 (and vice versa). We have verified that our plot preserves the intended data-model relation implied by the publicly available data; interested readers can independently verify this using those data. Similar plotting inversions have appeared in the literature, e.g., Figure 2 of Bond et al. (2017), as noted by Gould et al. (2023).

in our analysis are the same as those adopted by T22, except for the OGLE data, for which we re-reduced the OGLE-IV I -band data set. The OGLE-IV V -band data are used in Section 3 to measure the source color. The reported I - and V -band magnitudes have been calibrated onto the OGLE-III photometric system (Szymański et al. 2011) using common nearby field stars observed in both OGLE-IV and OGLE-III. The photometric uncertainties were rescaled following Yee et al. (2012) to ensure that the reduced χ^2 for each data set is unity.

A standard 2L1S model is characterized by seven parameters. In addition to the mass ratio q and the projected separation s , it includes the Paczyński parameters (Paczyński 1986): t_0 , u_0 , and t_E , which correspond to the time of closest approach of the source to a reference point in the lens system, the impact parameter in units of the angular Einstein radius θ_E , and the Einstein-radius crossing time, respectively. We adopt the magnification center as the reference point, using the definition in Z25. The sixth parameter, ρ , represents the angular source radius θ_* normalized by θ_E ($\rho = \theta_*/\theta_E$). The final parameter, α , is the angle between the source trajectory and the binary axis. For each data set i , we introduce two flux parameters, $f_{S,i}$ and $f_{B,i}$, to represent the source flux and blended flux, respectively.

We adopt the approach of Z25 to perform the 2L1S modeling, starting with a grid search and subsequently refining the parameters using the emcee ensemble sampler (Foreman-Mackey et al. 2013) and the Nelder-Mead simplex algorithm². We compute the 2L1S magnification using the most recent release of the advanced contour integration code VBMicrolensing (Bozza 2010; Bozza et al. 2018, 2025).

Neither the original discovery paper (Choi et al. 2012; hereafter C12) nor T22 explicitly stated whether limb-darkening effects for the source star were considered in the modeling. In our analysis, we explicitly include limb darkening. Based on the source properties in Section 3, we adopt linear limb-darkening coefficients from Claret & Bloemen (2011) appropriate for each observational bandpass.

Figure 2 presents the results of the grid search. Similar to the three events affected by the “Planet/Binary” degeneracy analyzed by Z25, OGLE-2011-BLG-0950 exhibits six “Binary” solutions. Following the nomenclature of Z25, we label the four cusps of the relevant diamond-shaped caustic as A–D and denote each solution by the consecutive cusp pair traversed by the source trajectory; we therefore label these solutions as “Close Binary AB”, “Close Binary BC”, “Wide Binary AB”, “Wide Binary BC”, “Wide Binary CD”, and “Wide Binary DA”. The corresponding caustic structures and

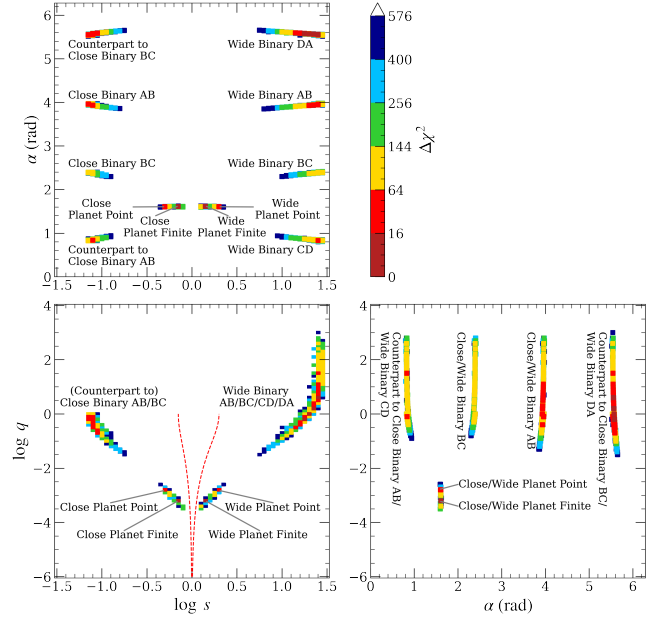


Figure 2. The χ^2 landscape in the $(\log s, \log q, \alpha)$ parameter space as explored by a grid search, following the approach described by Z25. Color coding is used to represent the statistical significance of grid points: dark red, red, yellow, green, blue, and dark blue correspond to deviations within $1n\sigma$, $2n\sigma$, $3n\sigma$, $4n\sigma$, $5n\sigma$, and $6n\sigma$, respectively, where $n = 4$. Grid points exceeding the $6n\sigma$ threshold are not shown. A total of 12 local minima are identified and labeled, two of which are redundant “counterpart” minima of other “Binary” solutions (i.e., intrinsically identical under the $q \leftrightarrow 1/q$ symmetry). The two red dashed lines mark the boundaries separating resonant and non-resonant caustic regimes, as defined by Equations (60) and (61) of Dominik (1999).

source trajectories are shown in Figure 3. We note that both C12 and T22 reported only two “Binary” solutions, which are the “Close Binary BC” and “Wide Binary DA” in our solutions.

For the planetary solutions, analogous to KMT-2022-BLG-0954 in Z25, we identify two pairs of solutions: one pair without finite-source effects (“Close Planet Point” and “Wide Planet Point”) and one pair with finite-source effects (“Close Planet Finite” and “Wide Planet Finite”). Among these, the “Planet Finite” solutions were the ones reported by C12 and T22. The “Planet Point” solutions were newly discovered. Figure 4 shows the combined MCMC chains for “Close Planet Finite” and “Close Planet Point”, demonstrating that the two solutions are indeed distinct.

Table 1 lists the 2L1S parameters for all solutions, as obtained from the MCMC. The “Planet Finite” solutions provide the best fit to the light curves. Among the “Binary” solutions, “Close Binary BC” and “Wide Binary DA” have the lowest χ^2 , but they are still disfavored relative to the “Planet Finite” solutions by $\Delta\chi^2 = 26$, which is consistent with the χ^2 difference reported by T22. The remaining “Binary” so-

² Implemented via `scipy.optimize.fmin`. See <https://docs.scipy.org/doc/scipy/reference/generated/scipy.optimize.fmin.html#scipy.optimize.fmin>

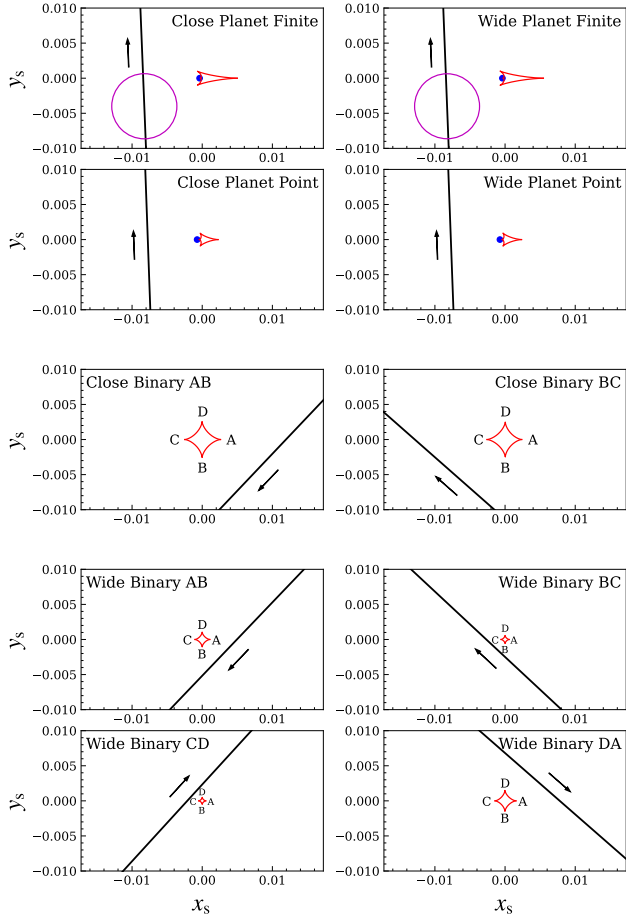


Figure 3. Caustic configurations for the ten 2L1S solutions listed in Table 1. In each panel, the caustic structure is shown by the red curves, the position of the primary lens is indicated by a blue dot, and the source-lens relative trajectory is plotted as a black line, with an arrow denoting the direction of source motion. For the two “Planet Finite” solutions, finite-source effects are detected, and the magenta circles indicate the angular radius of the source. For the six “Binary” solutions, individual caustic cusps are labeled as “A”, “B”, “C”, and “D”, according to the naming convention introduced by Z25.

lutions are even more disfavored, with $\Delta\chi^2$ ranging from 39 to 61.

The “Planet Point” solutions are disfavored by $\Delta\chi^2 = 48$, which appears statistically significant, but does not necessarily imply that they can be ruled out. Although the “Planet Finite” solutions are favored by $\Delta\chi^2 \geq 26$ relative to any other solutions, they are already excluded by the Keck AO observations reported by T22, which almost certainly indicates the presence of systematics in the light curves. As shown in the cumulative $\Delta\chi^2$ plot in Figure 1, the $\Delta\chi^2$ contributions for the “Close Binary BC” and “Close Planet Point” solutions originate from nearly the same regions, suggesting that both are affected by similar systematics. Therefore, the “Planet Point” solutions remain viable for this event.

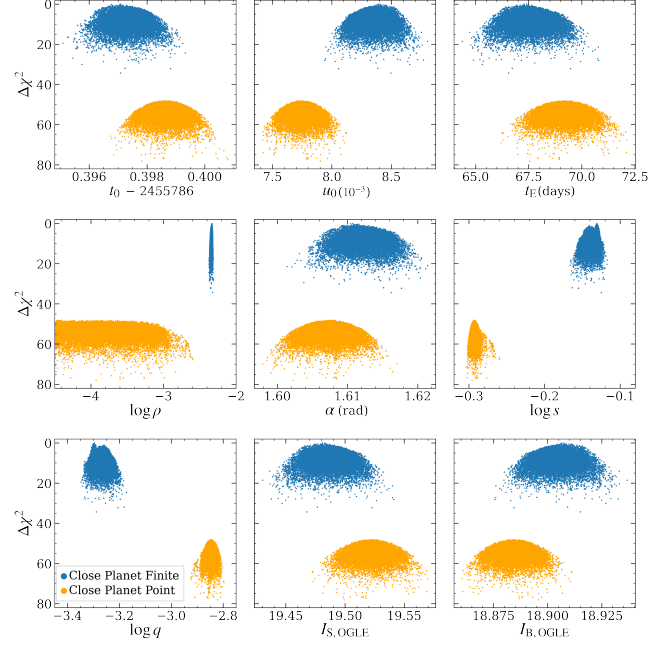


Figure 4. Combined MCMC chains for the “Close Planet Finite” (blue points) and “Close Planet Point” (orange points) solutions. The nine panels display the seven 2L1S parameters, as well as the source flux and blend flux in the OGLE-III magnitude system. The y-axis shows the $\Delta\chi^2$ of each point relative to the minimum χ^2 of the combined chains.

3. SOURCE PROPERTIES

We analyze the source properties in this section for three main reasons. First, the de-reddened source color and magnitude allow us to determine the angular source radius, θ_* , which (for the case that ρ is measured) can then be used to derive θ_E and the geocentric lens-source relative proper motion via

$$\theta_E = \frac{\theta_*}{\rho}, \quad \mu_{\text{rel},G} = \frac{\theta_E}{t_E}. \quad (1)$$

Different models may predict different values of $\mu_{\text{rel},G}$, which can be compared with the heliocentric lens-source relative proper motion, $\mu_{\text{rel},H}$, which was measured from the Keck AO imaging presented by T22, after accounting for the transformation between the geocentric and heliocentric frames, to validate or rule out the models.

Second, the de-reddened source color and magnitude enable us to infer the source apparent magnitude in the K_s -band of the Keck AO imaging through a color-color relation, thereby inferring which of the two stars resolved by Keck AO corresponds to the source and which to the lens. Third, the de-reddened source color can be used to estimate the effective temperature, T_{eff} , and thus to determine the limb-darkening coefficients adopted in the light-curve analysis.

3.1. Lens-Source Relative Proper Motion

Table 1. 2L1S Parameters for OGLE-2011-BLG-0950

Model	χ^2/dof	t_0 (HJD')	u_0 (10^{-3})	t_E (days)	ρ (10^{-3})	α (rad)	s	$\log q$	$I_{S,\text{OGLE}}$	
Close	Planet Finite	6992.3/6993	5786.3973	8.35	67.56	4.56	1.612	0.727	-3.271	19.486
			0.0005	0.11	0.80	0.08	0.002	0.011	0.024	0.014
	Planet Point	7040.5/6993	5786.3987	7.75	69.18	< 1.91	1.607	0.511	-2.849	19.522
			0.0005	0.09	0.74	—	0.002	0.006	0.016	0.012
Wide	Binary AB	7031.3/6993	5786.3972	8.65	64.46	< 2.69	3.954	0.073	-0.181	19.423
			0.0008	0.10	0.69	—	0.005	0.001	0.059	0.013
	Binary BC	7018.3/6993	5786.3974	8.51	65.20	< 2.63	2.419	0.075	0.314	19.436
			0.0006	0.11	0.75	—	0.006	0.002	0.068	0.013
Wide	Planet Finite	6992.4/6993	5786.3973	8.35	67.60	4.58	1.612	1.365	-3.270	19.487
			0.0005	0.11	0.81	0.08	0.002	0.021	0.024	0.014
	Planet Point	7040.6/6993	5786.3987	7.74	69.27	< 1.95	1.607	1.949	-2.845	19.523
			0.0005	0.10	0.80	—	0.002	0.017	0.014	0.013
Wide	Binary AB	7031.8/6993	5786.4018	3.85	145.56	< 1.58	3.948	25.065	0.605	19.426
			0.0005	0.30	11.15	—	0.003	0.477	0.088	0.013
	Binary BC	7053.4/6993	5786.3960	1.96	290.79	< 0.92	2.391	26.068	1.299	19.402
			0.0004	0.13	18.34	—	0.002	0.304	0.059	0.012
Wide	Binary CD	7045.4/6993	5786.3987	1.78	320.38	< 0.85	0.832	26.122	1.383	19.406
			0.0005	0.11	19.94	—	0.002	0.306	0.057	0.011
	Binary DA	7018.7/6993	5786.3932	5.28	105.29	< 1.74	5.566	22.214	0.198	19.437
			0.0005	0.34	6.77	—	0.004	0.914	0.099	0.013

NOTE. $\text{HJD}' = \text{HJD} - 2450000$. The parameters are reported with their 1σ uncertainties, while the upper limits on ρ corresponds to 3σ . The values of t_0 and u_0 are referenced to the magnification center, using the definition in Z25. The source magnitude is calibrated to the OGLE-III photometric system. The best-fit solution is highlighted in bold.

Based on the source color information from the SMARTS-CTIO V and I data and the OGLE-III color-magnitude diagram (CMD), T22 found a de-reddened source color of $(V - I)_{S,0} = 0.88 \pm 0.09$, and the subsequent source properties (e.g., θ_*) as well as $\mu_{\text{rel,G}}$ for different solutions are based on this value. For this event, a high-resolution spectrum was obtained using the Ultraviolet and Visual Echelle Spectrograph (UVES) on the Very Large Telescope (VLT) at a magnification of $A \sim 85$, i.e., close to the time of peak magnification, which showed that the source is a mildly evolved, metal-rich dwarf with an effective temperature of $T_{\text{eff}} = 6130 \pm 120$ K, a surface gravity of $\log g = 4.20 \pm 0.15$, a stellar mass of $M = 1.27^{+0.13}_{-0.07} M_{\odot}$, a metallicity of $[\text{Fe}/\text{H}] = +0.33 \pm 0.10$, and an age of $2.4^{+1.2}_{-0.8}$ Gyr (Bensby et al. 2013, 2017)³. This yields the intrinsic source color of $(V - I)_{S,0} = 0.60^{+0.04}_{-0.03}$, which is in strong tension with the CMD based color measurement of T22.

³ The full set of parameters of the source star is available in Table A.2 of Bensby et al. (2017) via VizieR: <https://vizier.cds.unistra.fr/viz-bin/VizieR-5?-ref=VIZ693fb9963b6bf&-out.add=&-source=J/A+A/605/A89/tablea2&recno=7>

To resolve this discrepancy, we include the OGLE-IV V -band data in the analysis and estimate the apparent source color as $(V - I)_S = 1.663 \pm 0.003$ based on a regression of OGLE-IV V against I flux as a function of magnification, followed by a calibration to the OGLE-III photometric system. We further analyze the OGLE-III $V - I$ versus I CMD using stars within $2.5'$ of the source position. The resulting CMD is shown in Figure 5. Applying the method of Nataf et al. (2013), we measure the observed centroid of the red clump (RC) to be $(V - I, I)_{\text{RC}} = (2.090 \pm 0.007, 15.872 \pm 0.031)$. We adopt the de-reddened color and magnitude of the RC as $(V - I, I)_{\text{RC},0} = (1.06 \pm 0.03, 14.55 \pm 0.04)$, taking $(V - I)_{\text{RC},0}$ from Bensby et al. (2013) and $I_{\text{RC},0}$ from Table 1 of Nataf et al. (2013), evaluated at the event longitude $l = -1.93^\circ$. Following

$$[E(V - I), A_I] = (V - I, I)_{\text{RC}} - (V - I, I)_{\text{RC},0}, \quad (2)$$

we derive the reddening and extinction toward the event to be $E(V - I) = 1.03 \pm 0.03$ and $A_I = 1.32 \pm 0.05$.

The source apparent magnitude I_S , which differs among the solutions, is listed in Table 1. Applying

$$(V - I, I)_{S,0} = (V - I, I)_S - [E(V - I), A_I], \quad (3)$$

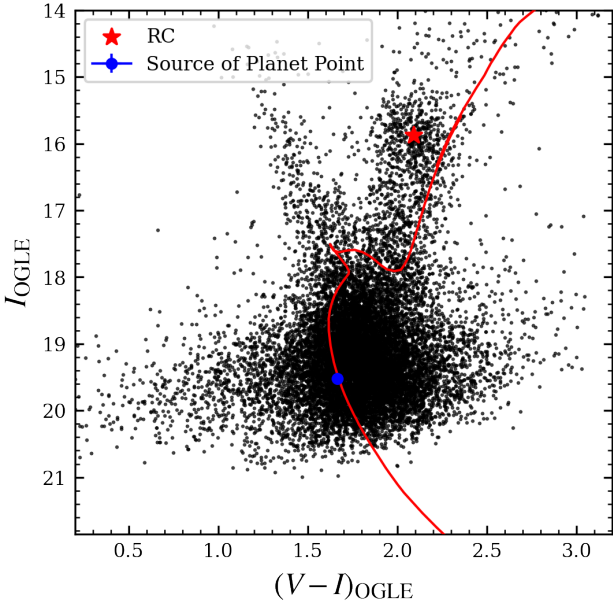


Figure 5. $V - I$ versus I color-magnitude diagram of OGLE-2011-BLG-0950 constructed from OGLE-III field stars (Szymański et al. 2011) within a $2.5'$ radius of the event. The red asterisk marks the centroid of the red clump (RC). The blue dot indicates the source position for the best-fit “Planet Point” solution, with its color derived from the OGLE-IV V - and I -band light curves. The red curve shows a PARSEC isochrone with an age of 2.4 Gyr, a $[M/H]$ of $+0.33$, and a distance of 9.2 kpc, adopting the same extinction as the RC. The age and metallicity are taken from the spectroscopic measurements of Bensby et al. (2013). The source properties inferred from the OGLE-IV light curves are consistent with these spectroscopic constraints.

we obtain a de-reddened source color of $(V - I)_{S,0} = 0.63 \pm 0.03$, which is consistent with the value inferred from the VLT spectrum. A comparison between our CMD analysis and that of T22 indicates that the primary difference arises from the adopted reddening value: we obtain $E(V - I) = 1.03 \pm 0.03$, whereas T22 adopted $E(V - I) = 0.83$. The reddening value used by T22 implies an extinction law of $A_I/E(V - I) = 1.6$, which is higher than typically observed values of $A_I/E(V - I) = 1.0\text{--}1.4$ toward the Galactic bulge (Figure 6 of Nataf et al. 2013). Because T22 adopted a redder intrinsic source color, the corresponding values of θ_* , θ_E and $\mu_{\text{rel},G}$ are overestimated, and the inferred source flux in the K_s -band is also overestimated.

Using the color-surface brightness relation of Adams et al. (2018),

$$\log(2\theta_*) = 0.378(V - I)_{S,0} + 0.542 - 0.2I_{S,0}, \quad (4)$$

we compute the angular source radius θ_* . θ_E and $\mu_{\text{rel},G}$ are then derived using Equation (1). The inferred θ_* , θ_E , and $\mu_{\text{rel},G}$ for different solutions are listed in Table 2.

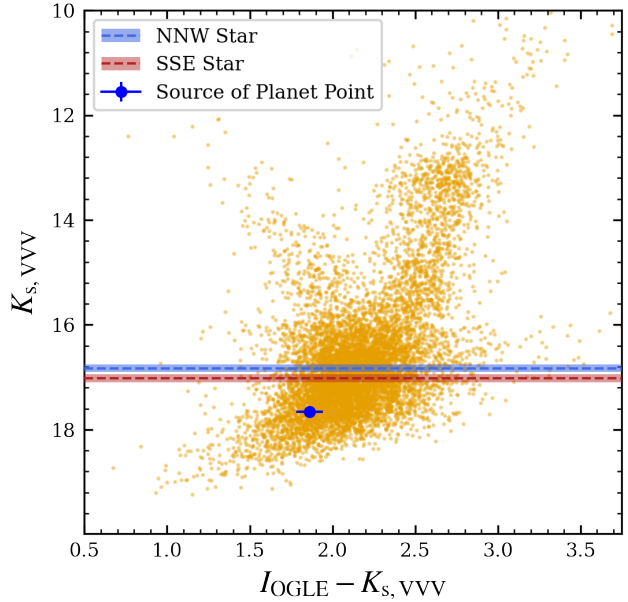


Figure 6. $I - K_s$ versus K_s CMD constructed from OGLE-III and VVV stars within a $2.5'$ radius of the event. The blue and red dashed lines indicate the magnitudes of the “NNW” and “SSE” stars identified in the Keck AO images, respectively, while the shaded bands indicate their 1σ uncertainties. The blue dot marks the position of the microlensed source star for the best-fit “Planet Point” solution.

Because the inferred lens-source relative proper motion for the “Planet Finite” solutions, $\mu_{\text{rel},G} = 0.83 \pm 0.04 \text{ mas yr}^{-1}$, is even lower than the value reported by T22, it is in stronger tension with the $\mu_{\text{rel},G} \simeq 4 \text{ mas yr}^{-1}$ obtained by converting the Keck AO heliocentric measurement of T22 to the geocentric frame. We therefore exclude the “Planet Finite” solutions. In contrast, the “Planet Point” and “Binary” solutions yield only lower limits on the relative proper motion, $\mu_{\text{rel},G} \gtrsim 1\text{--}2 \text{ mas yr}^{-1}$. They are therefore not excluded by the relative proper motion analysis. In addition, among the “Binary” solutions, the four “Wide Binary” are excluded because they would show a resolvable companion that is not seen in the Keck AO imaging (See Section 6 of T22). Thus, in the next section, we only derive the lens physical parameters for the “Planet Point” and “Close Binary” solutions.

3.2. Source and Lens Star Identification

To determine which of the two stars resolved in the Keck AO images by T22 corresponds to the source and which to the lens, we first estimate the source K_s -band magnitude, $K_{s,\text{Source}}$, using a color-color relation. From the CMD analysis in Section 3.1, we derive a de-reddened source color of $(V - I)_{S,0} = 0.63 \pm 0.03$. Using the color-color relation of Pecaut & Mamajek (2013), this corresponds to $(I - K_s)_{S,0} = 0.74 \pm 0.04$. Employing the relation of Kenyon & Hartmann (1995) yields a consistent value within 1σ . To estimate the extinction in the K_s band, we construct

Table 2. Derived θ_* , θ_E , $\mu_{\text{rel},G}$, and $K_{s,\text{Source}}$ for OGLE-2011-BLG-0950

Model	θ_*	θ_E	$\mu_{\text{rel},G}$	$K_{s,\text{Source}}$	
Unit	μas	mas	mas yr^{-1}	mag	
Close	Planet Finite	0.70 0.03	0.154 0.007	0.83 0.04	17.63 0.07
	Planet Point	0.69 0.03	> 0.362 —	> 1.91 —	17.66 0.07
	Binary AB	0.72 0.03	> 0.269 —	> 1.53 —	17.56 0.07
	Binary BC	0.72 0.03	> 0.274 —	> 1.53 —	17.58 0.07
	Planet Finite	0.70 0.03	0.154 0.007	0.83 0.04	17.63 0.07
	Planet Point	0.69 0.03	> 0.355 —	> 1.87 —	17.66 0.07
Wide	Binary AB	0.72 0.03	> 0.458 —	> 1.15 —	17.57 0.07
	Binary BC	0.73 0.03	> 0.795 —	> 1.00 —	17.54 0.07
	Binary CD	0.73 0.03	> 0.859 —	> 0.98 —	17.55 0.07
	Binary DA	0.72 0.03	> 0.414 —	> 1.43 —	17.58 0.07
	Planet Finite	0.70 0.03	0.154 0.007	0.83 0.04	17.63 0.07
	Planet Point	0.69 0.03	> 0.355 —	> 1.87 —	17.66 0.07

NOTE. The parameters are presented with their 1σ uncertainties. For the non-detection parameters, the 3σ lower limits are provided.

an $I_{\text{OGLE}} - K_{s,\text{VVV}}$ versus $K_{s,\text{VVV}}$ CMD using nearby field stars from the OGLE-III survey and the VISTA Variables in the Via Lactea (VVV) survey (Saito et al. 2012; Surot et al. 2019); see Figure 6. Applying the same method as described in Section 3.1, we derive a K_s -band extinction of $A_{K_s} = 0.20 \pm 0.04$, consistent with the extinction law relating A_{K_s} and A_I given by Nataf et al. (2016). For the “Planet Point” solutions, the inferred de-reddened source magnitude is $I_{S,0} = 18.20 \pm 0.05$, which implies

$$K_{s,\text{Source}} = I_{S,0} - (I - K_s)_{S,0} + A_{K_s} = 17.66 \pm 0.07. \quad (5)$$

Different solutions yield slightly different I_S and therefore slightly different $K_{s,\text{Source}}$, but the spread is only ~ 0.1 mag. The resulting $K_{s,\text{Source}}$ values for different solutions are listed in Table 2.

The Keck AO observations presented by T22 resolve two stars at the event position, with $K_{\text{SSE}} = 17.02 \pm 0.08$ and $K_{\text{NNW}} = 16.83 \pm 0.07$, where SSE and NNW denote the south-southeast and north-northwest stars, respectively. A

clear tension arises because our predicted source K_s -band magnitude is fainter than both the SSE and NNW stars by ~ 0.6 mag and ~ 0.8 mag for the “Planet Point” solutions and ~ 0.5 mag and ~ 0.7 mag for the “Close Binary” solutions. Therefore, in either configuration, the source star must have at least one unresolved companion contributing comparable K_s -band flux. We also note that our derived $K_{s,\text{Source}}$ is ~ 0.5 mag fainter than the value reported by T22. This difference is primarily due to their adoption of a redder intrinsic source color, which leads to an overestimate of the source K_s -band flux, as discussed in Section 3.1.

We next assess whether a binary source interpretation is compatible with both the microlensing light curve and the Keck AO images. As an illustrative example, we consider a second source with a relatively large impact parameter, $u_{0,2} \sim 5$. In this case, the second source would remain only weakly magnified and make a negligible contribution to the light curve, so that, together with the highly magnified primary source, the event could be well fitted by a single source model. Using the values of θ_E derived in Section 4, such a configuration corresponds to an angular separation of ~ 4 mas between the two sources. This is much smaller than the Keck AO point spread function (PSF) full width at half maximum (FWHM) of ~ 67 mas reported by T22, and hence the two sources would be unresolved in the AO images. We note that although this estimate is based on a single representative value of $u_{0,2}$, any configuration in which the second source passes several θ_E away from the lens would similarly satisfy both the light curve and imaging constraints. At the distance of the source, an angular separation of ~ 4 mas corresponds to a projected separation of ~ 40 au. For a $\sim 1.3 M_\odot$ source (as inferred from the VLT spectrum) with a companion of comparable mass, this separation implies an orbital period $\gtrsim 150$ yr, so any xallarap effect (Hardy & Walker 1995) on the microlensing light curve can safely be neglected.

Because the source star could be located at the position of either Keck star, both the NNW and SSE stars are, in principle, viable lens candidates. Using the Galactic model of Koshimoto et al. (2021) and the fact that the direction of $\mu_{\text{rel}} \equiv \mu_L - \mu_S$ flips when swapping the lens and source, T22 found that the NNW star is 3.79 times more likely to be the lens than the SSE star, although the latter possibility cannot be completely excluded. We therefore derive the lens physical parameters for two scenarios, one in which the NNW star is the lens and one in which the SSE star is the lens. However, the final inferred lens properties are only weakly sensitive to this choice, because the two stars have very similar K_s -band fluxes and will therefore yield similar lens masses and distances.

4. LENS PROPERTIES

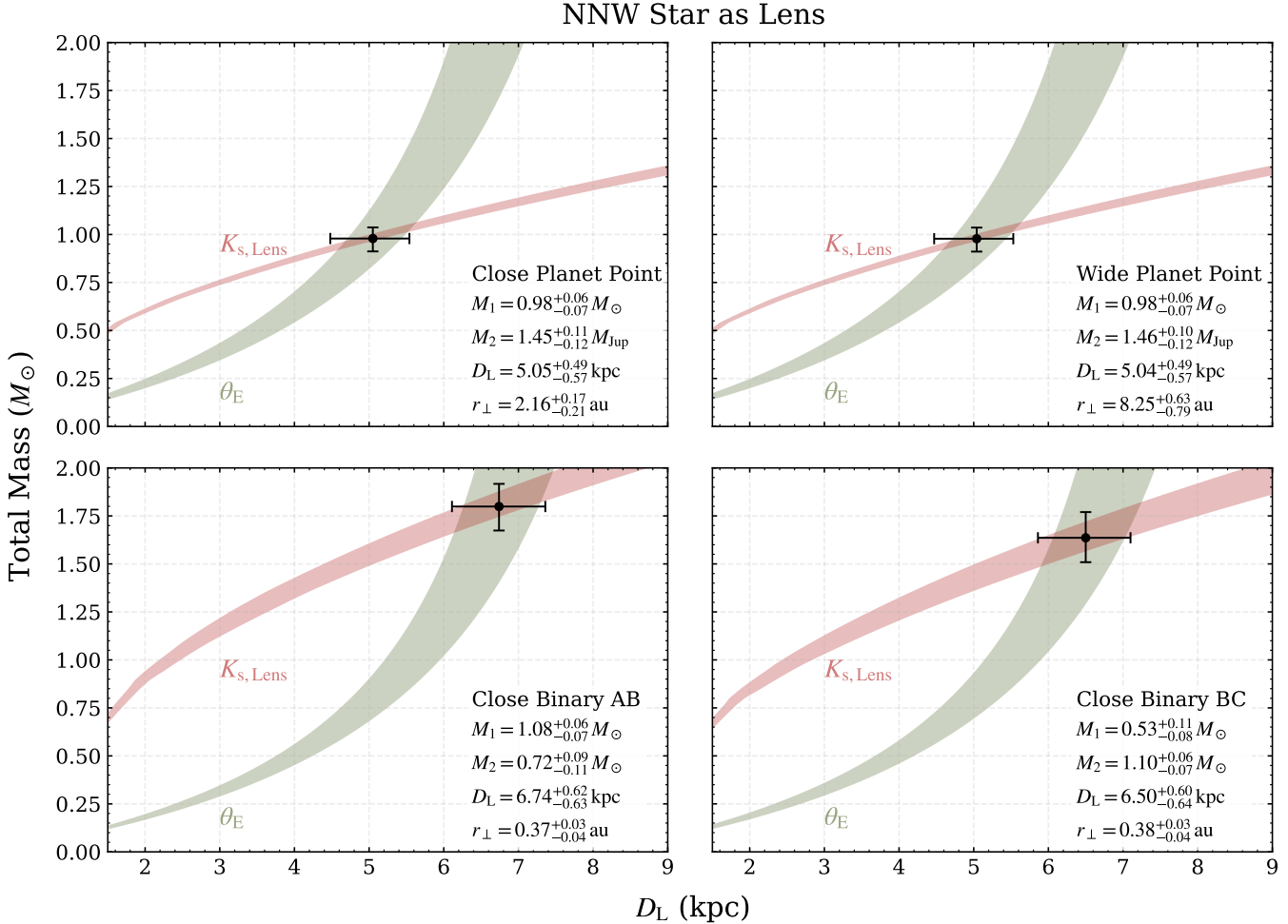


Figure 7. Constraints on the lens distance D_L and total lens mass $M_1 + M_2$ for the four viable 2L1S solutions of OGLE-2011-BLG-0950, assuming that the NNW star is the lens. In each panel, the green band shows the θ_E constraint derived from t_E and the Keck AO measurement of the lens-source relative proper motion, accounting for the uncertainties in θ_E and D_S . The red band shows the constraint from the Keck K_s -band lens flux using the empirical mass–luminosity relation, accounting for the uncertainties in the lens-flux measurement, extinction, and binary mass ratio. For the two “Close Binary” solutions, the Keck lens flux is interpreted as the combined flux of the two stellar components. The black point with 1σ error bars indicates the median values of $(D_L, M_1 + M_2)$ and their uncertainties from the forward modeling.

To determine the lens mass M_L and distance D_L , two independent mass-distance relations are required. For this event, one constraint is provided by the Keck AO observations, which yield a measurement of the lens brightness. A second relation arises from the connection between M_L , D_L , the angular Einstein radius θ_E , and the source distance D_S , given by

$$M_L = \frac{\theta_E^2}{\kappa \pi_{\text{rel}}}, \quad \pi_{\text{rel}} = \text{au} \left(\frac{1}{D_L} - \frac{1}{D_S} \right), \quad (6)$$

where $\kappa \equiv 4G/(c^2 \text{ au}) \simeq 8.144 \text{ mas } M_\odot^{-1}$, and π_{rel} is the lens-source relative parallax.

For this event, θ_E is obtained by combining the lens-source relative proper motion with the event time scale via Equation (1). However, the uncertainty in the source distance inferred from spectroscopy is relatively large, $D_S =$

$9.7^{+2.9}_{-1.4} \text{ kpc}$. Moreover, accurately propagating the uncertainties in all observables is most naturally done within a forward-modeling framework, which we adopt in the following analysis.

For each solution, we simulate 5×10^7 mock microlensing events. The source distances, D_S , are drawn from the Galactic model of Yang et al. (2021) and reweighted by the cumulative stellar density in front of the source to account for the higher microlensing probability of sources with more foreground stars, while lens masses, M_L , and distances, D_L , are sampled from uniform distributions. These quantities are then used to compute θ_E via Equation (6). We adopt an extinction profile along the line of sight based on the exponential dust distribution used by T22. Together with the empirical mass–luminosity relations from Henry & McCarthy (1993); Henry et al. (1999); Delfosse et al. (2000) used by

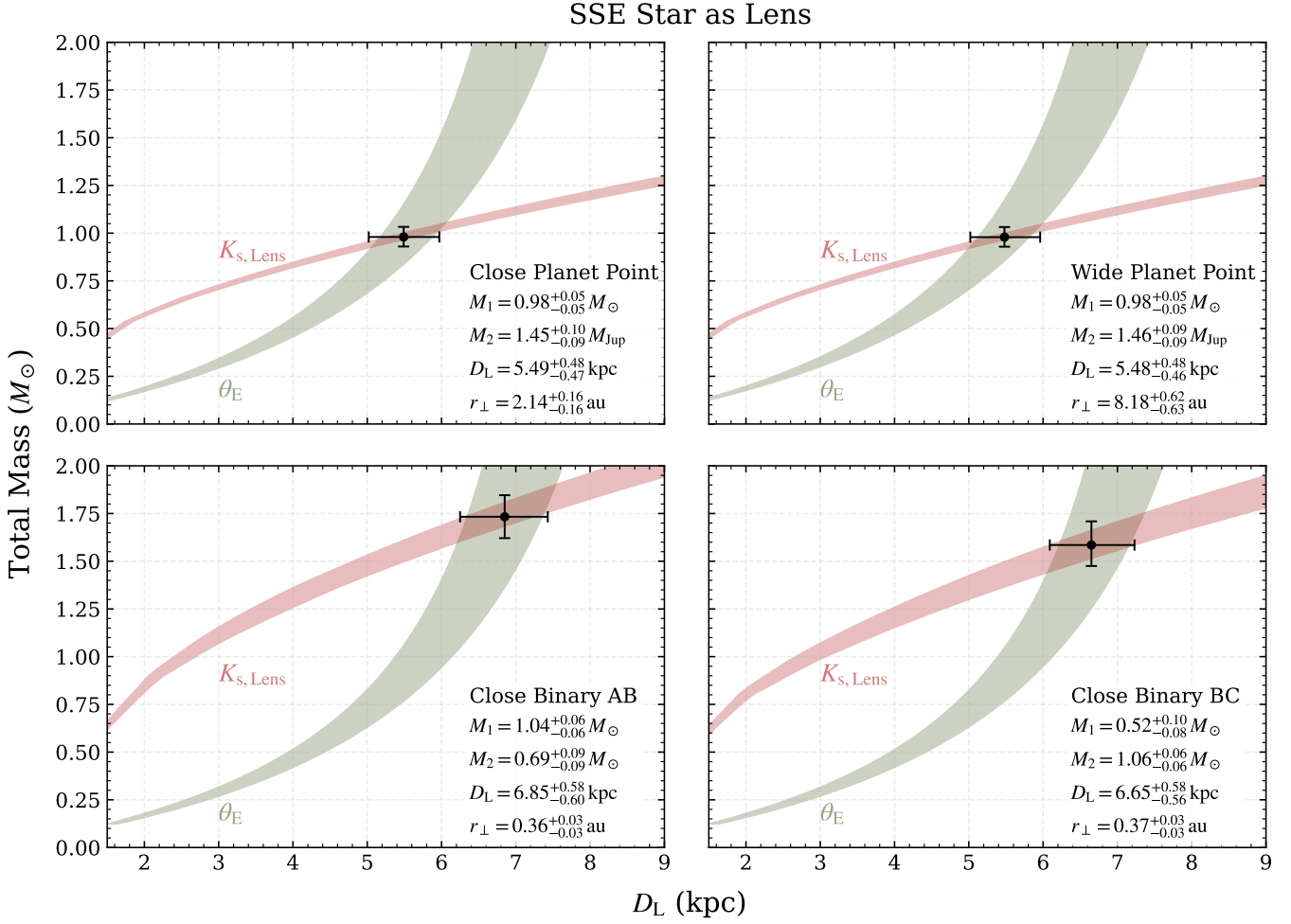


Figure 8. Same as Figure 7, but assuming that the SSE star is the lens. Because the SSE star is fainter than the NNW star and the SSE-star-as-lens scenario corresponds to a smaller $\mu_{\text{rel},G}$, hence a smaller θ_E , the allowed solutions shift to larger D_L .

T22, this allows us to derive the lens K_s -band magnitude, $K_{s,\text{Lens}}$. The impact of different modeling assumptions on the inferred lens properties is discussed in Section 5.

The heliocentric lens-source relative proper motion, $\mu_{\text{rel},H}$, is constrained by the Keck AO measurement. For each simulated event, we draw $\mu_{\text{rel},H}$ from the two-dimensional Gaussian likelihood defined by this measurement and then convert it to the geocentric frame via

$$\mu_{\text{rel},G} = \mu_{\text{rel},H} - \frac{v_{\oplus,\perp} \pi_{\text{rel}}}{\text{au}}, \quad (7)$$

where $v_{\oplus,\perp}$ is Earth’s projected velocity relative to the Sun at the time of peak magnification. The event time scale is then obtained using Equation (1). Finally, each simulated event is weighted by

$$w = p(t_E) \times p(K_{s,\text{Lens}}), \quad (8)$$

where $p(t_E)$ is the likelihood function for t_E derived from the light-curve analysis, and $p(K_{s,\text{Lens}})$ is the likelihood function for $K_{s,\text{Lens}}$ derived from the Keck AO observations.

Figures 7 and 8 show the constraints on M_L and D_L derived from the lens K_s -band magnitude and θ_E , assuming the NNW star to be the lens and the SSE star to be the lens, respectively. Table 3 summarizes the inferred physical parameters of the lens system, including D_S , D_L , $\mu_{\text{rel},G}$, and the component masses of the lens system, M_1 and M_2 , given by

$$M_1 = \frac{M_L}{1+q}, \quad M_2 = \frac{qM_L}{1+q}, \quad (9)$$

as well as the projected separation between the two lens components, r_{\perp} , and θ_E .

For the “Planet Point” solutions, the host is a solar-mass star and the companion is a super-Jupiter. Adopting a snow-line scaling of $r_{\text{SL}} = 2.7 \left(\frac{M_1}{M_{\odot}} \right)$ au (Kennedy & Kenyon 2008), the super-Jupiter lies well beyond the snow line in the “Wide” topology, whereas in the “Close” topology it is probably located near the snow line. For the “Close Binary” solutions, the more massive component is an F/G-type star, while the less massive component is likely a K-type star for the

Table 3. Lens Properties for OGLE-2011-BLG-0950

Lens	Solution	D_S (kpc)	D_L (kpc)	M_1 (M_\odot)	M_2 M_{Jup}	r_\perp (au)	$\mu_{\text{rel,G}}$ (mas yr $^{-1}$)	θ_E (mas)
NNW Star	Close Planet Point	$9.20^{+0.88}_{-0.89}$	$5.05^{+0.49}_{-0.57}$	$0.98^{+0.06}_{-0.07}$	$1.45^{+0.11}_{-0.12} M_{\text{Jup}}$	$2.16^{+0.17}_{-0.21}$	$4.44^{+0.24}_{-0.19}$	$0.84^{+0.05}_{-0.04}$
	Wide Planet Point	$9.21^{+0.88}_{-0.90}$	$5.04^{+0.49}_{-0.57}$	$0.98^{+0.06}_{-0.07}$	$1.46^{+0.10}_{-0.12} M_{\text{Jup}}$	$8.25^{+0.63}_{-0.79}$	$4.44^{+0.24}_{-0.19}$	$0.84^{+0.05}_{-0.04}$
	Close Binary AB	$9.23^{+0.89}_{-0.91}$	$6.74^{+0.62}_{-0.63}$	$1.08^{+0.06}_{-0.07}$	$0.72^{+0.09}_{-0.11} M_\odot$	$0.37^{+0.03}_{-0.04}$	$4.31^{+0.18}_{-0.17}$	$0.76^{+0.03}_{-0.03}$
	Close Binary BC	$9.23^{+0.86}_{-0.93}$	$6.50^{+0.60}_{-0.64}$	$0.53^{+0.11}_{-0.08}$	$1.10^{+0.06}_{-0.07} M_\odot$	$0.38^{+0.03}_{-0.04}$	$4.33^{+0.19}_{-0.18}$	$0.77^{+0.04}_{-0.03}$
SSE Star	Close Planet Point	$9.21^{+0.90}_{-0.88}$	$5.49^{+0.48}_{-0.47}$	$0.98^{+0.05}_{-0.05}$	$1.45^{+0.10}_{-0.09} M_{\text{Jup}}$	$2.14^{+0.16}_{-0.16}$	$4.04^{+0.15}_{-0.15}$	$0.76^{+0.03}_{-0.03}$
	Wide Planet Point	$9.22^{+0.90}_{-0.88}$	$5.48^{+0.48}_{-0.46}$	$0.98^{+0.05}_{-0.05}$	$1.46^{+0.09}_{-0.09} M_{\text{Jup}}$	$8.18^{+0.62}_{-0.63}$	$4.04^{+0.15}_{-0.15}$	$0.77^{+0.03}_{-0.03}$
	Close Binary AB	$9.24^{+0.89}_{-0.91}$	$6.85^{+0.58}_{-0.60}$	$1.04^{+0.06}_{-0.06}$	$0.69^{+0.09}_{-0.09} M_\odot$	$0.36^{+0.03}_{-0.03}$	$4.12^{+0.15}_{-0.15}$	$0.73^{+0.03}_{-0.03}$
	Close Binary BC	$9.24^{+0.86}_{-0.88}$	$6.65^{+0.58}_{-0.56}$	$0.52^{+0.10}_{-0.08}$	$1.06^{+0.06}_{-0.06} M_\odot$	$0.37^{+0.03}_{-0.03}$	$4.11^{+0.15}_{-0.15}$	$0.73^{+0.03}_{-0.03}$

“AB” solution and an M-type star for the “BC” solution. The projected separation is ~ 0.4 au. Compared to the “Planet Point” solutions, the “Close Binary” solutions favor a slightly more massive primary and a more distant lens system. This arises because the “Close Binary” solutions have a shorter event time scale and therefore a smaller θ_E . In addition, the θ_E of the more massive component is further reduced by a factor of $1/\sqrt{1+q}$. Because the lens flux is dominated by the more massive component, a smaller θ_E implies a higher lens mass and a larger distance for a given observed luminosity. In addition, when the NNW star (which is ~ 0.2 mag brighter) is assumed to be the lens, the larger derived $\mu_{\text{rel,G}}$ implies a larger θ_E , which in turn drives the solution toward a lens system that is closer to the Sun.

5. DISCUSSION

5.1. Implications for Roman Microlensing

The upcoming Nancy Grace Roman Space Telescope is expected to detect thousands of bound and free-floating planets through microlensing (Spergel et al. 2015; Penny et al. 2019; Johnson et al. 2020). One of Roman’s key advantages over ground-based microlensing surveys is its ability to resolve the lens and source for many events via multi-year, high-resolution imaging. Our discovery of new “Planet Point” solutions for OGLE-2011-BLG-0950, arising from the newly identified “Planet Finite/Planet Point” degeneracy and retaining consistency with the relative proper motion constraint from the Keck AO observations, indicates that the “Planet/Binary” degeneracy may still introduce substantial ambiguities in some Roman planetary events. Moreover, the fact that the “Planet Point” solutions for OGLE-2011-

BLG-0950 were not recognized in previous analyses highlights the need for caution when interpreting events affected by the “Planet/Binary” degeneracy.

Our revised analysis of the source properties reveals significant additional light at the source position, indicating that the source star has at least one companion. This represents the second microlensing event for which Keck AO imaging has shown that the source has a companion, with the other case being OGLE-2016-BLG-1195 (Shvartzvald et al. 2017; Bond et al. 2017; Gould et al. 2023; Vandorou et al. 2025). Current estimates of Roman’s capability to resolve the source and lens and to characterize the lens do not account for contamination from companions to the source or lens, nor from ambient field stars (Terry et al. 2025). Future analyses of Roman data will therefore need to carefully consider such contamination. In particular, if companions to the lens star contribute a significant fraction of the flux at the lens position but were not detected in the microlensing light curve, assuming a single lens star would bias the inferred host properties toward a more massive and more distant lens thereby affecting the derived planetary mass function, the inferred dependence of planet properties on their host stars, and the Galactic distributions of microlensing planets.

5.2. Dependence on Mass–Luminosity Relation

Previous treatments of the mass–luminosity relation in lens-flux analyses using Keck and the Hubble Space Telescope commonly adopt a single mass–luminosity relation (e.g., Bhattacharya et al. 2018), implicitly assuming that the adopted relation is only weakly sensitive to stellar age and metallicity. This approximation is generally adequate for

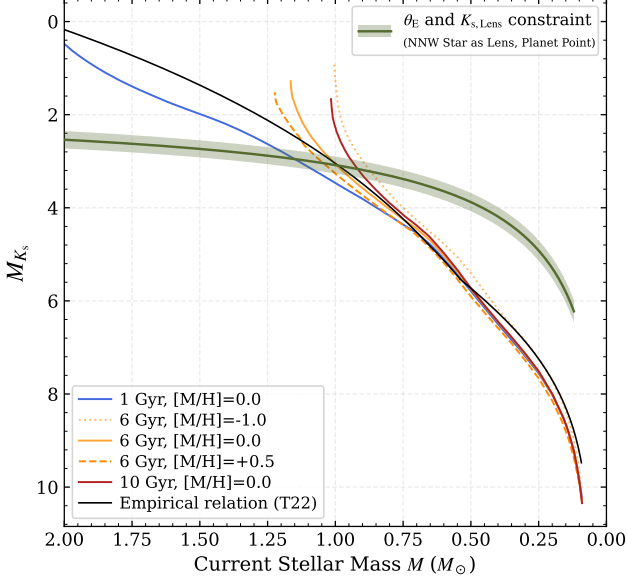


Figure 9. Comparison between the empirical and PARSEC mass-luminosity relations. The black curve shows the empirical mass-luminosity relation adopted by T22. Colored curves show PARSEC K_s -band isochrones (Bressan et al. 2012; Chen et al. 2014) for ages of 1, 6, and 10 Gyr and metallicities $[M/H] = -1.0, 0.0$, and $+0.5$. The green band shows the mass-luminosity constraint inferred from θ_E and Keck K_s -band lens flux for the “Planet Point” solutions with the NNW star taken as the lens, accounting for the uncertainties in θ_E , D_S , $K_{s,\text{Lens}}$, and extinction.

low-mass main-sequence lenses, for which the near-infrared mass–luminosity relation is nearly age/metallicity independent. However, for lenses with $M_L \gtrsim 1 M_\odot$, this assumption can break down as the lens approaches the turnoff/subgiant regime.

In this work, following T22, we adopt a single empirical mass–luminosity relation (Henry & McCarthy 1993; Henry et al. 1999; Delfosse et al. 2000), which does not account for the uncertainties in the mass–luminosity relation arising from variations in stellar age and metallicity. Figure 9 compares this empirical relation to five representative isochrones from the PAdova and tRieste Stellar Evolution Code (PARSEC) project (Bressan et al. 2012; Chen et al. 2014), together with the mass–luminosity constraint inferred from θ_E and Keck K_s -band lens flux. The empirical relation intersects the PARSEC isochrone with an age of 6 Gyr and a metallicity of $[M/H] = 0$ near the mass favored by the “Planet Point” solutions. Varying the age from 1 Gyr to 10 Gyr changes the inferred lens mass by $\sim 0.23 M_\odot$, which is larger than the reported 1σ uncertainty of $\sim 0.07 M_\odot$ listed in Table 3. Similarly, varying the metallicity from $[M/H] = -1.0$ to $+0.5$

results in a change in the inferred lens mass of $\sim 0.18 M_\odot$, again exceeding the uncertainty reported in Table 3. For the “Close Binary” solutions, the primary star alone is already more massive than the host in the “Planet Point” solutions. As a result, the same range of variations in stellar age and metallicity produce even larger shifts in the inferred lens mass. We therefore conclude that, for this event, the uncertainties in the lens properties are likely underestimated due to the simplified treatment of the mass–luminosity relations.

On the other hand, in the low-mass regime ($\lesssim 0.8 M_\odot$), the uncertainties in the mass–luminosity relation induced by variations in stellar age and metallicity are smaller, but may still be comparable to those arising from the θ_E constraint and the lens flux measurement.

Besides adopting a single mass–luminosity relation, some previous studies adopt the weighted isochrone distributions introduced by Bennett et al. (2018); however, these works do not explicitly compare the adopted age and metallicity distributions with observations, nor do they clearly describe how the weights are derived. The recently published code pyLIMASS (Bachelet et al. 2024) incorporates multiple isochrones but assigns equal weight to each isochrone. In addition, current treatments of the foreground extinction distribution often rely on simple analytic prescriptions (e.g., T22).

With the Gaia satellite (Gaia Collaboration et al. 2016, 2018), multi-band photometric surveys, and extensive spectroscopic campaigns, the Galactic distributions of stellar ages and metallicities (e.g., Anders et al. 2023), as well as the three-dimensional extinction distribution (e.g., Green et al. 2019), are now much better constrained. With Roman scheduled for launch in 2026/2027, it is therefore timely to develop a lens-flux analysis framework that incorporates realistically weighted isochrone distributions and improved models of foreground extinction. We are currently developing such a framework and will present it in a forthcoming work (Zhang et al., in preparation).

J.Z., W.Z., H.Y. and S.M. acknowledge support by the National Natural Science Foundation of China (Grant No. 12133005). The OGLE project has received funding from the Polish National Science Centre grant OPUS 2024/55/B/ST9/00447 awarded to A.U.. H.Y. acknowledges support by the China Postdoctoral Science Foundation (No. 2024M762938). This work is part of the ET space mission which is funded by the China’s Space Origins Exploration Program.

REFERENCES

Adams, A. D., Boyajian, T. S., & von Braun, K. 2018, MNRAS, 473, 3608, doi: [10.1093/mnras/stx2367](https://doi.org/10.1093/mnras/stx2367)

An, J. H. 2005, MNRAS, 356, 1409, doi: [10.1111/j.1365-2966.2004.08581.x](https://doi.org/10.1111/j.1365-2966.2004.08581.x)

Anders, F., Gispert, P., Ratcliffe, B., et al. 2023, *A&A*, 678, A158, doi: [10.1051/0004-6361/202346666](https://doi.org/10.1051/0004-6361/202346666)

Bachelet, E., Hundertmark, M., & Calchi Novati, S. 2024, *AJ*, 168, 24, doi: [10.3847/1538-3881/ad4862](https://doi.org/10.3847/1538-3881/ad4862)

Bennett, D. P., & Rhee, S. H. 1996, *ApJ*, 472, 660, doi: [10.1086/178096](https://doi.org/10.1086/178096)

Bennett, D. P., Udalski, A., Bond, I. A., et al. 2018, *AJ*, 156, 113, doi: [10.3847/1538-3881/aad59c](https://doi.org/10.3847/1538-3881/aad59c)

Bensby, T., Yee, J. C., Feltzing, S., et al. 2013, *A&A*, 549, A147, doi: [10.1051/0004-6361/201220678](https://doi.org/10.1051/0004-6361/201220678)

Bensby, T., Feltzing, S., Gould, A., et al. 2017, *A&A*, 605, A89, doi: [10.1051/0004-6361/201730560](https://doi.org/10.1051/0004-6361/201730560)

Bhattacharya, A., Beaulieu, J. P., Bennett, D. P., et al. 2018, *AJ*, 156, 289, doi: [10.3847/1538-3881/aaed46](https://doi.org/10.3847/1538-3881/aaed46)

Bond, I. A., Bennett, D. P., Sumi, T., et al. 2017, *MNRAS*, 469, 2434, doi: [10.1093/mnras/stx1049](https://doi.org/10.1093/mnras/stx1049)

Bozza, V. 2010, *MNRAS*, 408, 2188, doi: [10.1111/j.1365-2966.2010.17265.x](https://doi.org/10.1111/j.1365-2966.2010.17265.x)

Bozza, V., Bachelet, E., Bartolić, F., et al. 2018, *MNRAS*, 479, 5157, doi: [10.1093/mnras/sty1791](https://doi.org/10.1093/mnras/sty1791)

Bozza, V., Saggese, V., Covone, G., Rota, P., & Zhang, J. 2025, *A&A*, 694, A219, doi: [10.1051/0004-6361/202452648](https://doi.org/10.1051/0004-6361/202452648)

Bressan, A., Marigo, P., Girardi, L., et al. 2012, *MNRAS*, 427, 127, doi: [10.1111/j.1365-2966.2012.21948.x](https://doi.org/10.1111/j.1365-2966.2012.21948.x)

Cassan, A., Kubas, D., Beaulieu, J. P., et al. 2012, *Nature*, 481, 167, doi: [10.1038/nature10684](https://doi.org/10.1038/nature10684)

Chen, Y., Girardi, L., Bressan, A., et al. 2014, *MNRAS*, 444, 2525, doi: [10.1093/mnras/stu1605](https://doi.org/10.1093/mnras/stu1605)

Choi, J. Y., Shin, I. G., Han, C., et al. 2012, *ApJ*, 756, 48, doi: [10.1088/0004-637X/756/1/48](https://doi.org/10.1088/0004-637X/756/1/48)

Claret, A., & Bloemen, S. 2011, *A&A*, 529, A75, doi: [10.1051/0004-6361/201116451](https://doi.org/10.1051/0004-6361/201116451)

Delfosse, X., Forveille, T., Ségransan, D., et al. 2000, *A&A*, 364, 217, doi: [10.48550/arXiv.astro-ph/0010586](https://doi.org/10.48550/arXiv.astro-ph/0010586)

Dominik, M. 1999, *A&A*, 349, 108, <https://arxiv.org/abs/astro-ph/9903014>

Foreman-Mackey, D., Hogg, D. W., Lang, D., & Goodman, J. 2013, *PASP*, 125, 306, doi: [10.1086/670067](https://doi.org/10.1086/670067)

Gaia Collaboration, Prusti, T., de Bruijne, J. H. J., et al. 2016, *A&A*, 595, A1, doi: [10.1051/0004-6361/201629272](https://doi.org/10.1051/0004-6361/201629272)

Gaia Collaboration, Brown, A. G. A., Vallenari, A., et al. 2018, *A&A*, 616, A1, doi: [10.1051/0004-6361/201833051](https://doi.org/10.1051/0004-6361/201833051)

Gaudi, B. S. 1998, *ApJ*, 506, 533, doi: [10.1086/306256](https://doi.org/10.1086/306256)

Gaudi, B. S., & Gould, A. 1997, *ApJ*, 486, 85, doi: [10.1086/304491](https://doi.org/10.1086/304491)

Gould, A., & Loeb, A. 1992, *ApJ*, 396, 104, doi: [10.1086/171700](https://doi.org/10.1086/171700)

Gould, A., Shvartzvald, Y., Zhang, J., et al. 2023, *AJ*, 166, 145, doi: [10.3847/1538-3881/aced3c](https://doi.org/10.3847/1538-3881/aced3c)

Gould, A., Dong, S., Gaudi, B. S., et al. 2010, *ApJ*, 720, 1073, doi: [10.1088/0004-637X/720/2/1073](https://doi.org/10.1088/0004-637X/720/2/1073)

Green, G. M., Schlafly, E., Zucker, C., Speagle, J. S., & Finkbeiner, D. 2019, *ApJ*, 887, 93, doi: [10.3847/1538-4357/ab5362](https://doi.org/10.3847/1538-4357/ab5362)

Griest, K., & Safizadeh, N. 1998, *ApJ*, 500, 37, doi: [10.1086/305729](https://doi.org/10.1086/305729)

Han, C., & Gaudi, B. S. 2008, *ApJ*, 689, 53, doi: [10.1086/592723](https://doi.org/10.1086/592723)

Hardy, S. J., & Walker, M. A. 1995, *MNRAS*, 276, L79, doi: [10.1093/mnras/276.1.L79](https://doi.org/10.1093/mnras/276.1.L79)

Henry, T. J., Franz, O. G., Wasserman, L. H., et al. 1999, *ApJ*, 512, 864, doi: [10.1086/306793](https://doi.org/10.1086/306793)

Henry, T. J., & McCarthy, Jr., D. W. 1993, *AJ*, 106, 773, doi: [10.1086/116685](https://doi.org/10.1086/116685)

Johnson, S. A., Penny, M., Gaudi, B. S., et al. 2020, *AJ*, 160, 123, doi: [10.3847/1538-3881/aba75b](https://doi.org/10.3847/1538-3881/aba75b)

Kennedy, G. M., & Kenyon, S. J. 2008, *ApJ*, 673, 502, doi: [10.1086/524130](https://doi.org/10.1086/524130)

Kenyon, S. J., & Hartmann, L. 1995, *ApJS*, 101, 117, doi: [10.1086/192235](https://doi.org/10.1086/192235)

Koshimoto, N., Baba, J., & Bennett, D. P. 2021, *ApJ*, 917, 78, doi: [10.3847/1538-4357/ac07a8](https://doi.org/10.3847/1538-4357/ac07a8)

Mao, S., & Paczynski, B. 1991, *ApJL*, 374, L37, doi: [10.1086/186066](https://doi.org/10.1086/186066)

Nataf, D. M., Gould, A., Fouqué, P., et al. 2013, *ApJ*, 769, 88, doi: [10.1088/0004-637X/769/2/88](https://doi.org/10.1088/0004-637X/769/2/88)

Nataf, D. M., Gonzalez, O. A., Casagrande, L., et al. 2016, *MNRAS*, 456, 2692, doi: [10.1093/mnras/stv2843](https://doi.org/10.1093/mnras/stv2843)

Paczynski, B. 1986, *ApJ*, 304, 1, doi: [10.1086/164140](https://doi.org/10.1086/164140)

Pecaut, M. J., & Mamajek, E. E. 2013, *ApJS*, 208, 9, doi: [10.1088/0067-0049/208/1/9](https://doi.org/10.1088/0067-0049/208/1/9)

Penny, M. T., Gaudi, B. S., Kerins, E., et al. 2019, *ApJS*, 241, 3, doi: [10.3847/1538-4365/aafb69](https://doi.org/10.3847/1538-4365/aafb69)

Poleski, R., Skowron, J., Mróz, P., et al. 2021, *AcA*, 71, 1, doi: [10.32023/0001-5237/71.1.1](https://doi.org/10.32023/0001-5237/71.1.1)

Saito, R. K., Hempel, M., Minniti, D., et al. 2012, *A&A*, 537, A107, doi: [10.1051/0004-6361/201118407](https://doi.org/10.1051/0004-6361/201118407)

Shvartzvald, Y., Maoz, D., Udalski, A., et al. 2016, *MNRAS*, 457, 4089, doi: [10.1093/mnras/stw191](https://doi.org/10.1093/mnras/stw191)

Shvartzvald, Y., Yee, J. C., Calchi Novati, S., et al. 2017, *ApJL*, 840, L3, doi: [10.3847/2041-8213/aa6d09](https://doi.org/10.3847/2041-8213/aa6d09)

Spergel, D., Gehrels, N., Baltay, C., et al. 2015, arXiv e-prints, arXiv:1503.03757. <https://arxiv.org/abs/1503.03757>

Surot, F., Valenti, E., Hidalgo, S. L., et al. 2019, *A&A*, 629, A1, doi: [10.1051/0004-6361/201935730](https://doi.org/10.1051/0004-6361/201935730)

Suzuki, D., Bennett, D. P., Sumi, T., et al. 2016, *ApJ*, 833, 145, doi: [10.3847/1538-4357/833/2/145](https://doi.org/10.3847/1538-4357/833/2/145)

Szymański, M. K., Udalski, A., Soszyński, I., et al. 2011, *AcA*, 61, 83. <https://arxiv.org/abs/1107.4008>

Terry, S. K., Bennett, D. P., Bhattacharya, A., et al. 2022, *AJ*, 164, 217, doi: [10.3847/1538-3881/ac9518](https://doi.org/10.3847/1538-3881/ac9518)

Terry, S. K., Bachelet, E., Zohrabi, F., et al. 2025, arXiv e-prints, arXiv:2510.13974, doi: [10.48550/arXiv.2510.13974](https://doi.org/10.48550/arXiv.2510.13974)

Vandorou, A., Dang, L., Bennett, D. P., et al. 2025, AJ, 169, 319,
doi: [10.3847/1538-3881/adcec2](https://doi.org/10.3847/1538-3881/adcec2)

Yang, H., Mao, S., Zang, W., & Zhang, X. 2021, MNRAS, 502,
5631, doi: [10.1093/mnras/stab441](https://doi.org/10.1093/mnras/stab441)

Yee, J. C., Shvartzvald, Y., Gal-Yam, A., et al. 2012, ApJ, 755, 102,
doi: [10.1088/0004-637X/755/2/102](https://doi.org/10.1088/0004-637X/755/2/102)

Zang, W., Jung, Y. K., Yee, J. C., et al. 2025, Science, 388, 400,
doi: [10.1126/science.adn6088](https://doi.org/10.1126/science.adn6088)

Zhang, J., Zang, W., Ryu, Y.-H., et al. 2025, MNRAS,
doi: [10.1093/mnras/staf1893](https://doi.org/10.1093/mnras/staf1893)